

Intertwining of Frustration with Magneto-Elastic Coupling in the Multiferroic LuMnO₃

Shin-ichiro Yano^{1*}, Despina Louca¹, Songxue Chi², Masaaki Matsuda²,
Yiming Qiu^{3,4}, John R. D. Copley^{3,4}, and Sang-Wook Cheong⁵

¹University of Virginia, Department of Physics, Charlottesville, VA 22904, U.S.A.

²Quantum Condensed Matter Division, Oak Ridge National Laboratory, Oak Ridge, TN 37831, U.S.A.

³NIST Center for Neutron Research, NIST, Gaithersburg, MD 20899-8102, U.S.A.

⁴Department of Materials Science and Engineering, University of Maryland, College Park, MD 20742, U.S.A.

⁵Rutgers Center for Emergent Materials and Department of Physics and Astronomy, Rutgers University, Piscataway, NJ 08854, U.S.A.

(Received July 20, 2013; accepted November 11, 2013; published online December 25, 2013)

Residual magnetic frustration in the multiferroic LuMnO₃ may be key towards understanding magneto-elastic coupling in hexagonal manganites. Critical magnetic scattering present well above the magnetic ordering temperature T_N persists below, as observed by inelastic neutron scattering. The magnetic fluctuations are confined in two dimensions implied by the characteristic wavevector dependence of the magnetic structure factor that changes from symmetric to asymmetric across T_N . The low dimensionality of the magnetic structure is also evident in the temperature dependence of the commensurate antiferromagnetic intensity which follows a mean field exponent of $\beta \sim 0.2$.

1. Introduction

For nearly a decade, multiferroics of the kind that exhibit successive ferroelectric and magnetic orders have captivated the research community in large part due to their unique properties.^{1–4} Central to this field has been the nature of the competing magnetic interactions and their coupling to the ferroelectric degree of freedom. Among the different types of multiferroics discovered thus far, one of the earliest examples investigated is that of the hexagonal RMnO₃ with the $P6_3cm$ space group (R : rare earth ion with small radius such as Y, Lu, Ho, and Yb).^{5–7} While ferroelectricity sets in around 1000 K, antiferromagnetic (AFM) order materializes at a much lower temperatures, in the vicinity of $T_N \sim 100$ K. Coupling between the two orders is implied by the observation of a dielectric anomaly near the AFM transition⁸) but the lack of an apparent lattice distortion at that temperature indicates that the magneto-elastic coupling is weak. The Mn³⁺ ions with a total spin $S = 2$ form a triangular lattice in the ab -plane where the Mn spins are coupled indirectly through the oxygen atoms. With the crystal structure shown in Fig. 1(a), a stack of two planes at $z = 0$ and $1/2$ creates a hexagonal Mn sublattice as shown in Fig. 1(b), where the Mn spins nominally order in-plane, oriented in a 120° configuration in the so-called Γ_4 structure. Even though the Mn³⁺ ions are coupled antiferromagnetically, their triangular arrangement is not without frustration. It is most likely due to strong frustration that LuMnO₃ does not order until 86 K yielding a frustration index, the ratio between the Curie–Weiss temperature, θ_{CW} , to T_N of about 10.3,⁸) an extremely high ratio in comparison to other known frustrated magnets, such as the spinels.⁹) Thus, given the degree of magnetic frustration and the big disparity in the two ordering temperatures, T_C and T_N , the coupling between the two order parameters is in question. LuMnO₃ is an ideal system through which the intertwining of magnetic frustration and ferroelectricity can be explored.

A plethora of studies on the hexagonal manganites focused on YMnO₃.^{10–13}) Earlier neutron diffraction results provided evidence for strong diffuse scattering superimposed on the

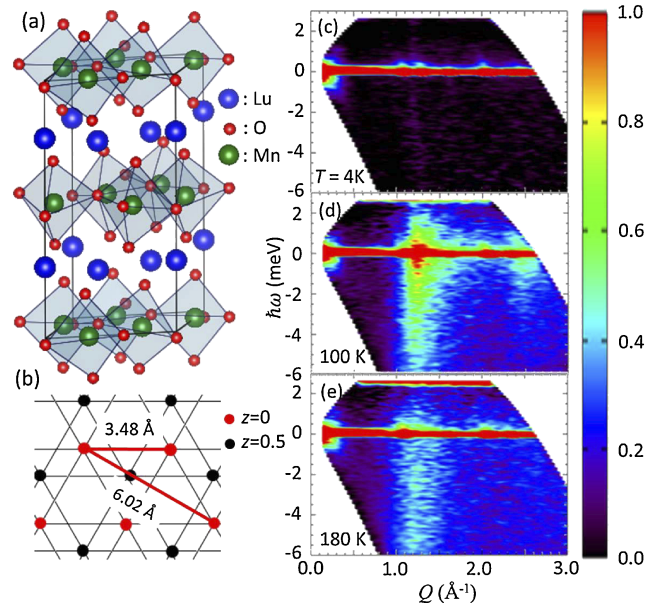


Fig. 1. (Color online) (a) The crystal structure of LuMnO₃ with the space symmetry of $P6_3cm$. (b) The hexagonal lattice of the Mn atom alone formed by overlaying two layers along the z -direction. (c) The neutron scattering contour maps of energy (E) versus momentum transfer (Q) at 4 K, (d) at 100 K, and (e) at 180 K.

nuclear and magnetic structures. By effectively removing the static component from the diffraction pattern, a modulation is evident in reciprocal space, with a broad peak appearing at a momentum transfer, $Q \approx 1.15 \text{ \AA}^{-1}$, which corresponds to a (100) nuclear peak.¹¹) Elastic neutron scattering on a single crystal of LuMnO₃ also showed the presence of diffuse scattering intensity at $Q \approx 1.20 \text{ \AA}^{-1}$ corresponding to the (100) reflection. The intensity was highly anisotropic, as it was very broad in the $(1, 0, l)$ direction and much sharper in the $(h, 0, 0)$ direction and reached a maximum at T_N .¹⁴) The (100) reflection is where the minimum of the spin wave dispersion occurs. It has been previously suggested that the local symmetry in LuMnO₃ is lower than the reported $P6_3cm$ due to the enhanced tilting of the MnO₅ bipyramids, creating

three unique Mn–O bonds in the plane. The $P6_3$ symmetry can better describe the local structure¹⁵⁾ and this may be significant in the magnetic interactions. Unlike in YMnO_3 , no single-ion anisotropy is present in LuMnO_3 ¹⁶⁾ and the interlayer superexchange is weaker,¹⁴⁾ but in this paper we show that nearest- and next-nearest-neighbor Mn interactions rise above the frustration to establish interplane coupling well above T_N .

Our neutron scattering results on LuMnO_3 show how the scattering intensity under the (100) and (200) reflections changes from elastic to inelastic as a function of temperature in going through the transition. Critical magnetic scattering appears at temperatures well above the AFM transition, and precipitously disappears below as the system globally orders. The inelastic scattering, although broad, appears in the same region in momentum space as the (100) and (200) reflections. Its shape is symmetric as it follows a liquid-like structure factor above T_N , but becomes *asymmetric* in going through T_N before it disappears at base temperature. Meanwhile, the evolution of the commensurate magnetic phase transition follows a mean-field temperature dependence with a critical exponent, β , of about 0.2, suggesting that the AFM interactions are two dimensional in nature as well, and confined in the plane.

2. Experiment

Elastic and inelastic neutron scattering measurements were performed on a single crystal and a powder sample of LuMnO_3 as a function of temperature. About 40 g of powder was prepared by a standard solid-state reaction method from Lu_2O_3 and MnO_2 . The single crystal of about 0.4 g was grown using the traveling floating zone method. The procedure is described elsewhere.^{17,18)} Using the Wide Angle Neutron Diffractometer (WAND) at the High Flux Isotope Reactor (HFIR) of Oak Ridge National Laboratory, scans in the $(h0l)$ and $(hk0)$ scattering planes were performed. The wavelength was set at $\lambda = 1.48 \text{ \AA}$ by using a vertically focusing Ge(113) monochromator. This instrument is equipped with a curved, one-dimensional ^3He position sensitive detector that allows access to a wide region in reciprocal space. A detailed temperature dependence was carried out in the vicinity of the $(101)_{\text{AFM}}$ Bragg reflection to determine the order parameter. The inelastic neutron scattering measurements were carried out at the Disk Chopper Spectrometer (DCS) at the NIST Center for Neutron Research (NCNR) using the powder sample. The wavelength was set to $\lambda = 4.5 \text{ \AA}$ which yields a range in $Q = 0.12$ to 2.6 \AA^{-1} at the elastic line and the full width at half maximum of the elastic line, $\Delta E/E = 0.14 \text{ meV}$.

3. Results

In Figs. 1(c)–1(e), the neutron scattering intensity is plotted as a contour map of energy versus momentum transfer, E – Q , at three temperatures, 4, 100, and 200 K, for the data collected from the DCS. The bright red bar corresponds to the elastic line with nearly zero energy transfer. A strong inelastic scattering intensity is clearly visible, emanating from two Q points, $Q \approx 1.20$ and 2.40 \AA^{-1} , extending well into the inelastic regime. The scattering is asymmetric in Q and exhibits a strong temperature dependence as can be seen from a comparison between the three contour maps. Barely present at 4 K, the scattering

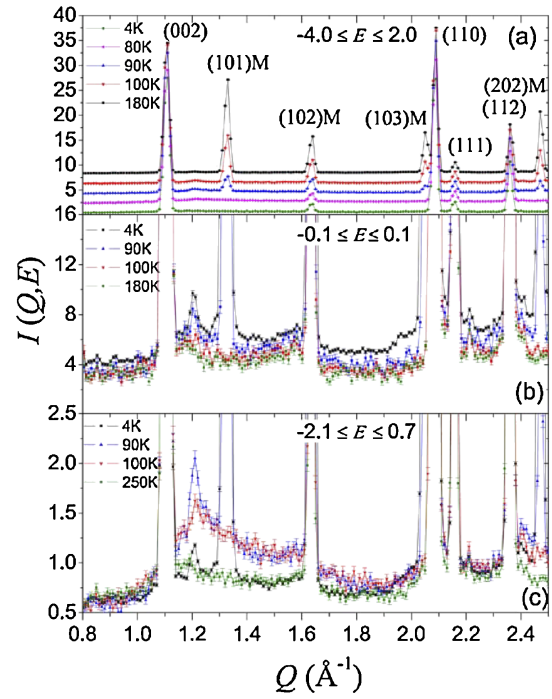


Fig. 2. (Color online) The temperature dependence of the scattering intensity, $I(Q, \omega)$, plotted at three different energy cuts. In (a), the energy was integrated from -4.0 to 2.0 meV which includes a large portion of the inelastic as well as all the elastic scattering. The (M) indicates magnetic peaks. In (b), the energy was integrated from -0.1 to 0.1 meV which is predominantly elastic. The $(100)_{\text{FM}}$ peak around $Q = 1.20 \text{ \AA}^{-1}$ is clearly visible. In (c), the energy was integrated from -2.1 to 0.7 meV . The $(200)_{\text{FM}}$ peak becomes visible in this cut.

intensifies by 100 K and then subsides by 200 K. Cuts across in energy within an energy window yield the integrated intensity, shown in Fig. 2. In Fig. 2(a), a broad energy integration is performed, including the elastic line, from -4.0 to 2.0 meV . Just like in a conventional diffraction experiment, we can observe both magnetic and nuclear Bragg reflections as labeled in the figure. The scale on the y-axis is linear. Shown in this figure are data collected at five different temperatures, above and below $T_N \sim 90 \text{ K}$. The magnetic structure corresponds to the Γ_4 magnetic pattern as described in earlier works.^{8,14,15)} In Fig. 2(b), a much finer energy integration is performed, from -0.1 to 0.1 meV , well within the resolution of the elastic line in the current experimental setup. In the plot of $I(Q, E_{\text{integrated}})$, an additional weak (100) Bragg reflection becomes evident among the existing reflections. This peak is observed amidst the rising inelastic scattering with cooling and is most intense by 4 K, but absent above 100 K. By expanding the integration limits across -2.1 to 0.7 meV , a second reflection is identified, the (200) as indicated in the panel, in addition to the (100). The (200) is also present in panel (b) but it is much weaker, while in panel (c), it is clearly identified. Both peaks reside on top of a very distinctly broad inelastic scattering with the intensity maximum culminating at $Q = 1.20$ and 2.40 \AA^{-1} . The reflections and inelastic intensity must have the same origin.

Turning the attention to the inelastic intensity alone, Figs. 3(a)–3(d) are plots of the integrated intensity at a constant energy range of -2.7 to -0.3 meV as a function of temperature. By excluding the elastic portion of the scattering, only the inelastic spectrum is integrated, without

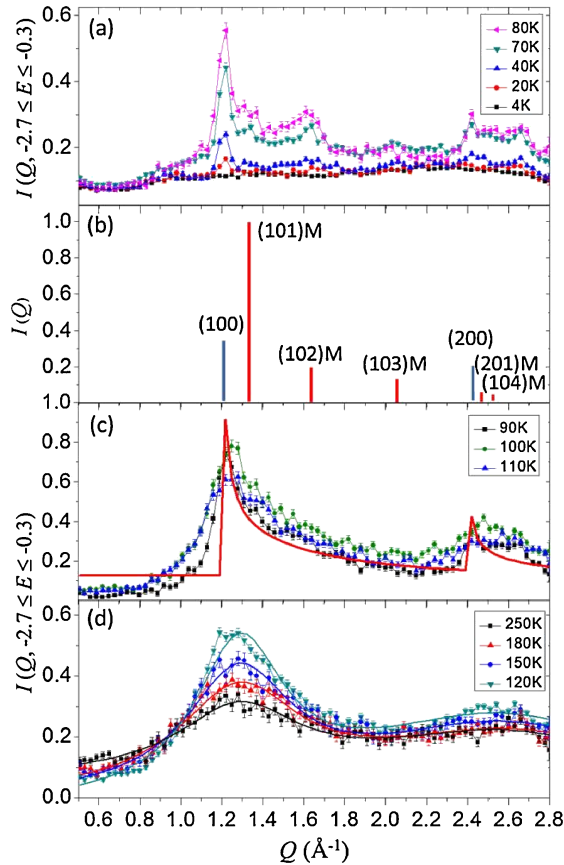


Fig. 3. (Color online) The scattering intensity $I(Q, \omega)$ integrated from $-2.5 \leq E \leq -0.3$ meV, is shown in three temperature regions. In (a), the temperatures are below T_N . In (c), they are slightly above T_N . The asymmetric function is most distinct around T_N and it is fit by a 2D Warren function for 90 K (solid line) in (d), the temperatures are well above T_N . The scattering function is fit by two Lorentzian functions. Shown in (b), are lines positioned at the appropriate Q 's to mark the magnetic peak positions for comparison purposes. The blue lines correspond to the forbidden reflections and the red lines correspond to the commensurate reflections.

the Bragg peaks. Distinct differences in the inelastic spectra are observed above and below T_N . Firstly, below T_N , the overall shape of the integrated intensity is asymmetric while above T_N , it is symmetric. In Fig. 3(a), at the lowest temperature of 4 K, the intensity is absent, indicating that the scattering is all in the elastic channels. As the temperature is raised to 40 K, scattering is initially observed at $Q \sim 1.20 \text{ \AA}^{-1}$ that gets stronger as the temperature goes up. Additional weaker peaks are observed as well at other regions in Q as the temperature rises, and have the same Q as the corresponding Bragg reflections shown in Fig. 3(b). The decrease in the intensity as a function of Q follows the magnetic form factor. Secondly, on approaching T_N from below as shown in Fig. 3(c), the spin fluctuations show a drastic change where the intensity function is clearly asymmetric, with a sharp increase at low Q , in a way that is analogous to magnetic correlations arising from systems with reduced dimensionality. Note that the strongest Q modulation corresponds to the same Q as the (100) Bragg reflection. A second broad peak is centered at the Q corresponding to the (200) reflection. Thirdly, just above T_N , the structure function shows the most asymmetry but the step-like feature of the structure function softens while the intensity starts to decrease at 100 K and beyond. The 90 K

data are fit by the two-dimensional (2D) Warren function.¹⁹⁾ By increasing the temperature, it can clearly be seen that the intensity spreads out while it is decreasing, and the shape becomes more symmetric. The intensity can be fit by two Lorentzians in this case. Critical scattering is present well above the transition in this system. We now turn our attention to understand the origin of the asymmetry on approaching T_N and of the inelastic intensity in the magnetically ordered state. Where do the magnetic fluctuations come from?

4. Discussion

The strong inelastic neutron scattering intensity observed at $Q \approx 1.20$ and at the less intense Q point of 2.40 \AA^{-1} correspond to nearest neighbor ($\sim 3.48 \text{ \AA}$) and next nearest neighbor ($\sim 6.52 \text{ \AA}$) Mn–Mn spin correlations as shown in Fig. 1(a). Similar features have been observed in geometrically frustrated magnetic materials such as in CuCrO_2 ,²⁰⁾ and ZnV_2O_4 ²¹⁾ where an asymmetric inelastic intensity was observed with only a single peak corresponding to nearest neighbors. Such asymmetry is indicative of a lower dimensionality, characteristic of the magnetic interactions. In YMnO_3 ,¹¹⁾ although a similar modulation at one Q point was observed by comparing diffraction data above and below T_N and looking at the diffuse scattering, no asymmetry was observed and given that the data were obtained from a diffraction experiment, the origin of the diffuse scattering was undetermined. In addition, the doping dependence of spin lattice coupling and two dimensional ordering was studied in $\text{Y}_{1-x}\text{Lu}_x\text{MnO}_3$. In this system, the spin–spin correlation length decreases with Lu doping. The correlation length in LuMnO_3 is the shortest.²²⁾ However, the fact that these inelastic features exist in a wide temperature range in the LuMnO_3 suggests that strong magnetic correlations beyond nearest neighbor Mn atoms exist well above T_N . The inelastic integrated intensity under the two modulations is shown in Fig. 4(a) as a function of temperature. Both Q modulations follow the same temperature dependence, with a steep decline right above T_N , and then gradually going to zero below as the intensity shifts from the inelastic to the elastic channels. From this figure it is clear that the intensity is present well above T_N , almost three times larger than T_N . Below T_N , the (100) and (200) reflections arise as the spin fluctuations freeze and the intensity transfers from the inelastic to the elastic component. This suggests that FM fluctuations are present well above T_N , that gradually freeze as static FM coupling is established with cooling. The intensity of the (100) and (200) peaks is extremely small in comparison with the other magnetic peaks. The fact that the inelastic intensity is present all the way down to 40 K indicates that fluctuations persist well below T_N , and that the system remains frustrated even after magnetic ordering sets in.

The asymmetry in the structure function suggests that the fluctuations are confined in the Mn plane and lack a c -axis component. Further support of the two dimensional character of the spin correlations is provided by the temperature dependence of the (101)_{AFM} Bragg peak. From data collected on WAND using the single crystal, the integrated intensity of the elastic scattering at (101) as a function of temperature is shown in Fig. 4(b). The magnetic intensity at (101) follows a power law dependence, $I \propto |(T/T_N) - 1|^{2\beta}$ with β obtained from the fitting and evaluated to be $\beta = 0.20$, a value that is

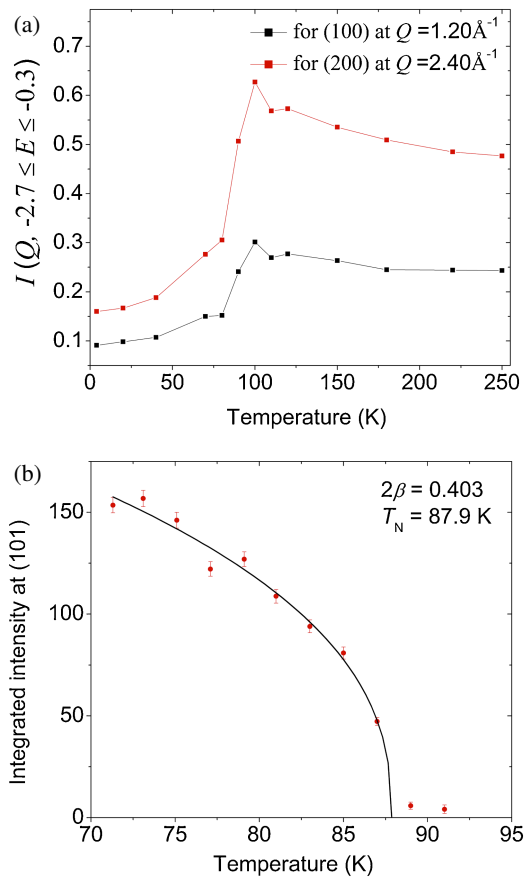


Fig. 4. (Color online) (a) The integrated intensity of the two broad inelastic peaks shown in Fig. 3. (b) Fitting of the (101)_{AFM} peak intensity obtained from WAND.

typical of 2D antiferromagnets. The transition temperature was determined as $T_N = 87.9 \pm 0.7 \text{ K}$. Typical 2D antiferromagnets [BaNi₂(PO₄)₂] has a magnetization exponent that correspond to the expected theoretical value $\beta = 0.23$.²³⁾ We note that $\beta = 0.187(2)$ in YMnO₃.¹²⁾

The triangular Mn sublattice allows for the residual frustration most likely due to the local MnO₅ distortions. As we previously showed, the O4 crystal site splits to two, creating a fifth oxygen site, O5. This lowers the local symmetry from $P6_3cm$ to $P6_3$ where all glide and mirror planes are eliminated. The superexchange between the nearest Mn atoms is mediated by the intermediate oxygen atoms via the near 120° Mn–O–Mn channel but given that there are three types of Mn–O–Mn as the O4 site splits to two, the bond angles are different particularly below T_N .¹⁵⁾ The Mn–O4–Mn and Mn–O5–Mn with similar angles are separated from the Mn–O3–Mn bond angle. This indicates that there are two similar in magnitude J constants and a very different third one. At the same time, the c -axis off-center displacements of the O3, O4, and O5 atoms are significant in the electric polarization since they are bonded to Lu. The electric polarization in the $P6_3$ unit cell is only allowed along the c -axis as in the $P6_3cm$ symmetry which is parallel to the sixfold screw axis, while all in-plane polarizations cancel each other out.

5. Conclusion

To conclude, the highly entropic state arising from the magnetic frustration in LuMnO₃ leads to a low Néel temperature. When entropy is reduced by lowering the

temperature, the magnetic interaction energy wins and the fluctuations freeze giving rise to a static structure, albeit complex. In the case of LuMnO₃, magnetic frustration is most likely present well below T_N , with fluctuations confined in the plane. This seems to be a quite common feature in this class of materials.

Acknowledgments

The authors would like to acknowledge A. Athauda and B. Li for their help with the experiment and S.-H. Lee for valuable discussions. This work is supported by the U.S. Department of Energy under contracts DE-FG02-01ER45927 at the University of Virginia and by DE-FG02-07ER46382 at Rutgers. The NCNR DCS is supported by the National Science Foundation under contract DMR-0944772. The research at the High Flux Isotope Reactor at ORNL was sponsored by the Scientific User Facilities Division, Office of Basic Energy Sciences, U.S. Department of Energy.

*sy3a@virginia.edu

- 1) T. Kimura, *Annu. Rev. Mater. Res.* **37**, 387 (2007).
- 2) H. Katsura, N. Nagaosa, and A. V. Balatsky, *Phys. Rev. Lett.* **95**, 057205 (2005).
- 3) S.-W. Cheong and M. Mostovoy, *Nat. Mater.* **6**, 13 (2007).
- 4) T.-h. Arima, *J. Phys. Soc. Jpn.* **80**, 052001 (2011).
- 5) S. Lee, A. Pirogov, M. Kang, K.-H. Jang, M. Yonemura, T. Kamiyama, S.-W. Cheong, F. Gozzo, N. Shin, H. Kimura, Y. Noda, and J.-G. Park, *Nature* **451**, 805 (2008).
- 6) M. C. Lin, Y. S. Chen, T. C. Han, J. G. Lin, and C. H. Chen, *Ferroelectrics* **380**, 38 (2009).
- 7) J.-S. Zhou, J. B. Goodenough, J. M. Gallardo-Amores, E. Morán, M. A. Alario-Franco, and R. Caudillo, *Phys. Rev. B* **74**, 014422 (2006).
- 8) T. Katsufuji, S. Mori, M. Masaki, Y. Moritomo, N. Yamamoto, and H. Takagi, *Phys. Rev. B* **64**, 104419 (2001); T. Katsufuji, M. Masaki, A. Machida, M. Moritomo, K. Kato, E. Nishibori, M. Takata, M. Sakata, K. Ohoyama, K. Kitazawa, and H. Takagi, *Phys. Rev. B* **66**, 134434 (2002).
- 9) A. P. Ramirez, *Annu. Rev. Mater. Sci.* **24**, 453 (1994).
- 10) A. Muñoz, J. A. Alonso, M. J. Martínez-Lope, M. T. Casáis, J. L. Martínez, and M. T. Fernández-Díaz, *Phys. Rev. B* **62**, 9498 (2000).
- 11) J. Park, J.-G. Park, G. S. Jeon, H.-Y. Choi, C. Lee, W. Jo, R. Bewley, K. A. McEwen, and T. G. Perring, *Phys. Rev. B* **68**, 104426 (2003).
- 12) B. Roessli, S. N. Gvasaliya, E. Pomjakushina, and K. Conder, *JETP Lett.* **81**, 287 (2005).
- 13) T. Chatterji, S. Ghosh, A. Singh, L. P. Regnault, and M. Rheinstädter, *Phys. Rev. B* **76**, 144406 (2007).
- 14) H. J. Lewtas, A. T. Boothroyd, M. Rotter, D. Prabhakaran, H. Müller, M. D. Le, B. Roessli, J. Gavilano, and P. Bourges, *Phys. Rev. B* **82**, 184420 (2010).
- 15) P. Tong, D. Louca, N. Lee, and S.-W. Cheong, *Phys. Rev. B* **86**, 094419 (2012).
- 16) I. V. Solovyev, M. V. Valentyuk, and V. V. Mazurenko, *Phys. Rev. B* **86**, 054407 (2012).
- 17) A. Ghosh, J. R. Sahu, S. V. Bhat, and C. N. R. Rao, *Solid State Sci.* **11**, 1639 (2009).
- 18) A. B. Souchkov, J. R. Simpson, M. Quijada, H. Ishibashi, N. Hur, J. S. Ahn, S. W. Cheong, A. J. Millis, and H. D. Drew, *Phys. Rev. Lett.* **91**, 027203 (2003).
- 19) B. E. Warren, *Phys. Rev.* **59**, 693 (1941).
- 20) M. Poirier, F. Damay, C. Martin, J. Robert, and S. Petit, *Phys. Rev. B* **81**, 104411 (2010).
- 21) S.-H. Lee, D. Louca, H. Ueda, S. Park, T. J. Sato, M. Isobe, Y. Ueda, S. Rosenkranz, P. Zschack, J. Íñiguez, Y. Qiu, and R. Osborn, *Phys. Rev. Lett.* **93**, 156407 (2004).
- 22) J. Park, S. Lee, M. Kang, K.-H. Jang, C. Lee, S. V. Streltsov, V. V. Mazurenko, M. V. Valentyuk, J. E. Medvedeva, T. Kamiyama, and J.-G. Park, *Phys. Rev. B* **82**, 054428 (2010).
- 23) S. T. Bramwell and P. C. W. Holdsworth, *J. Phys.: Condens. Matter* **5**, L53 (1993).